

An apparatus for measuring nonlinear viscoelasticity of minerals at high temperature

Cite as: Rev. Sci. Instrum. **92**, 073902 (2021); <https://doi.org/10.1063/5.0035699>

Submitted: 30 October 2020 . Accepted: 18 June 2021 . Published Online: 08 July 2021

 Ri Cao,  Lars N. Hansen,  Christopher A. Thom, and  David Wallis



View Online



Export Citation



CrossMark

ARTICLES YOU MAY BE INTERESTED IN

[Embedded gas sensing setup for air samples analysis](#)

Review of Scientific Instruments **92**, 074102 (2021); <https://doi.org/10.1063/5.0050445>

[Influence of Rogowski coil structure for sub-ns current pulses](#)

Review of Scientific Instruments **92**, 073303 (2021); <https://doi.org/10.1063/5.0050201>

[Breakthrough instruments and products: An integrated instrument for enhanced, highly precise Hall effect measurement and analysis of electronic materials](#)

Review of Scientific Instruments **92**, 069501 (2021); <https://doi.org/10.1063/5.0057103>

 QBLOX



1 qubit

Shorten Setup Time
Auto-Calibration
More Qubits

Fully-integrated
Quantum Control Stacks
Ultrastable DC to 18.5 GHz
Synchronized <<1 ns
Ultralow noise



100s qubits

[visit our website >](#)

An apparatus for measuring nonlinear viscoelasticity of minerals at high temperature

Cite as: *Rev. Sci. Instrum.* **92**, 073902 (2021); doi: [10.1063/5.0035699](https://doi.org/10.1063/5.0035699)

Submitted: 30 October 2020 • Accepted: 18 June 2021 •

Published Online: 8 July 2021



View Online



Export Citation



CrossMark

Ri Cao,¹  Lars N. Hansen,^{2,a)}  Christopher A. Thom,¹  and David Wallis³ 

AFFILIATIONS

¹ Department of Earth Sciences, University of Oxford, Oxford OX1 3AN, United Kingdom

² Department of Earth and Environmental Sciences, University of Minnesota, Minneapolis, Minnesota 55455, USA

³ Department of Earth Sciences, University of Cambridge, Cambridge CB2 3EQ, United Kingdom

^{a)} Author to whom correspondence should be addressed: lnhansen@umn.edu

ABSTRACT

We describe a high-temperature, uniaxial creep apparatus designed to investigate nonlinear attenuation of materials over a wide range of temperatures (25–1300 °C) using forced oscillations combined with a bias stress. This apparatus is primarily designed for investigation of minerals and rocks with high melting temperatures. An oscillatory compressional stress is used to determine attenuation and Young's modulus at frequencies of 10^{-1} – 10^2 Hz and high stress amplitudes (>0.1 MPa). Large bias stresses are applied in addition to the oscillatory stresses such that attenuation tests are conducted simultaneously with the ongoing creep. The complex compliance of the apparatus was characterized by conducting calibration tests on orientated crystals of sapphire. The real part of the apparatus compliance exhibits a dependence on sample length and frequency, whereas the imaginary part is only dependent on frequency. The complex compliance is not dependent on the oscillation amplitude or the bias stress. We assess the accuracy and precision of this calibration by comparing measurements of the attenuation and Young's modulus of aluminum and acrylic to previously published values. We outline a set of criteria defining the conditions over which this apparatus can precisely determine the attenuation and Young's modulus of a sample based on the sample length and expected values of attenuation and Young's modulus.

Published under an exclusive license by AIP Publishing. <https://doi.org/10.1063/5.0035699>

I. INTRODUCTION

Viscoelasticity describes the mechanical properties of materials that exhibit both viscous and elastic behavior, with the relative proportion of the two depending on the timescale of observation (Lakes, 2009). Rocks clearly exhibit viscoelastic behavior as they act elastically on very short timescales and viscously on very long timescales. Many previous investigations of viscoelasticity in geological materials have focused on seismological properties, such as seismic-wave attenuation (Cline *et al.*, 2018; Farla *et al.*, 2012; Jackson and Faul, 2010; McCarthy *et al.*, 2011; and Takei *et al.*, 2011), and therefore have been conducted at low stress amplitudes (corresponding to $<10^{-5}$ in elastic strain) in the linear regime. However, increasingly complex viscoelastic phenomena may occur as stress amplitudes are increased and the behavior becomes nonlinear. For nonlinear viscoelastic materials, the relationship between the magnitude of a perturbation in stress and the magnitude of the resulting strain is nonlinear, given a fixed time or

frequency (Lakes, 2009, chapter 2.12). Nonlinear viscoelasticity likely characterizes the response of the solid earth in situations with abrupt and substantial stress changes, such as post-seismic relaxation (Agata *et al.*, 2019; Freed *et al.*, 2012; Masuti *et al.*, 2016; Moore *et al.*, 2017; and Qiu *et al.*, 2018).

Unfortunately, currently available apparatuses have a variety of limitations for investigating nonlinear viscoelasticity in geological materials. Typical viscoelastic measurements of geological materials have been performed by applying a periodic stress that oscillates symmetrically between positive and negative stresses, that is, the time-averaged stress or bias stress is zero (Gribb and Cooper, 1998a; Jackson and Paterson, 1993; Li and Weidner, 2007; and Sundberg and Cooper, 2010). However, nonlinear viscoelasticity in crystalline materials tends to arise from the dynamics of lattice dislocations. The dislocation density and any internal stress fields scale with the quasi-static applied stress (Bai and Kohlstedt, 1992 and Twiss, 1986), and therefore, if the time-averaged stress is negligible, then there is a tendency for initial dislocation densities to reduce and internal

stresses to relax. Some researchers have predeformed samples under a quasi-static stress in a separate apparatus to induce high dislocation densities prior to attenuation tests at elevated temperatures (Farla *et al.*, 2012). Temperatures in these tests are kept at moderate levels to prevent dislocation recovery, but although dislocation densities may not change dramatically during the subsequent attenuation test, the internal stresses still likely relax substantially and rapidly due to modest rearrangements of the dislocations (Wallis *et al.*, 2020).

Application of a non-zero bias stress during oscillation tests overcomes some of these difficulties. A quasi-static bias stress maintains dislocation densities and internal stress levels throughout superimposed oscillation tests (e.g., Sapozhnikov and Kustov, 1997). Application of very large quasi-static bias stresses, such that the material is actively creeping during simultaneous oscillations, also allows dislocation dynamics to be investigated through features such as the acoustoplastic effect (e.g., Kaiser and Pechhold, 1969). Furthermore, Gremaud *et al.* (1987) demonstrated that superimposing low-amplitude forced oscillations on top of large-amplitude, low-frequency oscillations of a bias stress can allow one to uniquely identify the aspects of the dislocation dynamics contributing to energy dissipation. Thus, future investigations of nonlinear viscoelasticity in geological materials will greatly benefit from being able to apply a controlled, non-zero bias stress during attenuation measurements. We note that several existing apparatus (McCarthy and Cooper, 2016 and Takei *et al.*, 2011) have been designed for geological applications that can apply a controlled bias stress during oscillatory experiments. However, they are limited to low temperatures typically used to investigate geological materials with very low melting temperatures (e.g., ice) or organic compounds that are reasonable analogs for geological materials (e.g., borneol).

Here, we introduce a novel apparatus specifically designed to overcome the limitations of existing apparatus. This new apparatus is based on traditional, high-temperature, uniaxial dead-load rigs designed for creep tests under controlled environments. The key modification of traditional designs is the addition of a piezoelectric actuator for applying oscillating loads. This actuator allows us to apply a controlled bias stress while simultaneously applying a superimposed oscillatory stress. Here, we describe the main features of the apparatus and outline a series of calibration experiments to define the range of material properties that can be explored.

II. APPARATUS

A. Loading frame and actuation

Figure 1 depicts the key components of the uniaxial deformation apparatus. The primary loading frame consists of two steel sheets with cutouts for access points. An upper crosshead is fixed in place and acts as a mounting point for a water-cooled bracket that holds the upper SiC piston. The bottom SiC piston is mounted in series with a piezoelectric actuator and a load cell. SiC pistons are 20 mm in diameter. The load cell sits atop a steel piston with a flange such that the piston can be supported in one of two ways. First, as depicted in Fig. 1(b), a collar that is driven by a worm gear mounted on the lower crosshead can transfer the load from

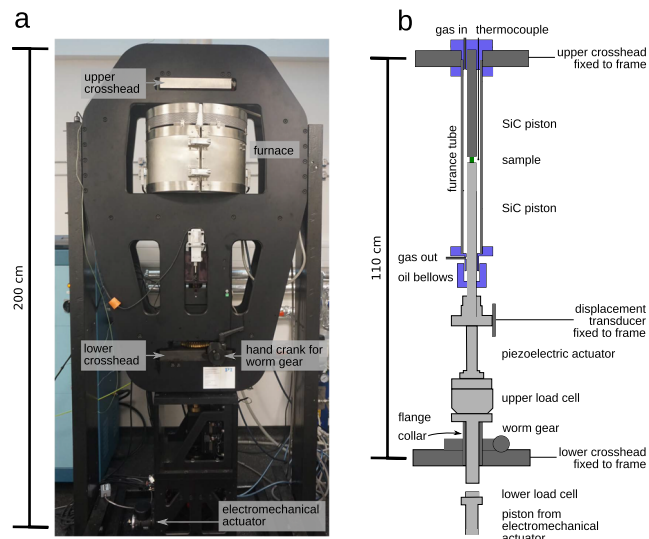


FIG. 1. High-temperature uniaxial creep apparatus for investigation of viscoelastic properties. (a) Photograph of the apparatus in the Rock Rheology Lab at the University of Oxford with annotations of key visible features. (b) Schematic illustration of the primary components of the loading column. Dark-gray components are fixed to the loading frame. Blue components are water cooled. The displacement transducer (a linear encoder) measures displacement of the light-gray components relative to the dark-gray components. The electromechanical actuator is decoupled from the loading column in the pictured configuration, and the collar is fully raised to support the flanged piston, transferring load to the lower crosshead.

the loading column to the lower crosshead and frame if the collar is high enough to come in contact with the flange on the steel piston. Alternatively, a central piston that goes through the collar can be loaded from below by the lower electromechanical actuator. This configuration transfers the load to the electromechanical actuator and its mounting points at the base of the main loading frame.

In the first configuration, the electromechanical actuator is effectively removed from the system, and the lower SiC piston is primarily driven by the piezoelectric actuator. The piezoelectric actuator (model P-025.80P produced by Physik Instrumente) is set up in a closed control loop with the upper load cell to enable maintenance of constant loads. A strain gauge is affixed to the piezoelectric actuator to monitor the available throw of the actuator (a maximum of $\sim 180 \mu\text{m}$). If the piezoelectric actuator runs out of throw, then the collar, steel piston, load cell, and piezoelectric actuator can all be driven upward by hand using the worm gear. Because of the fast response of the control loop, this hand adjustment can be made while a constant load is being maintained. In the second configuration, the loading column is driven by the electromechanical actuator, which has a total throw of $\sim 3 \text{ cm}$. This ball-screw driven actuator is configured for actuation to be controlled by position or displacement rate and is solely used for producing traditional measurements of yield and flow stress at strains $> 10^{-3}$. The rest of this article is focused on measurements of viscoelasticity using the first configuration.

B. Displacement and load measurement

Figure 1 also depicts the critical components for measuring sample displacement and the applied load. The primary displacement transducer is a linear encoder, with the readhead mounted on the loading column just above the load cell and the encoded scale mounted on the loading frame, providing a measurement of displacement of the bottom of the loading column (and therefore the bottom SiC piston) relative to the loading frame. Flexural motion of the piston is not currently accounted for but could be addressed with future placement of multiple transducers around the piston. Displacement is measured at a resolution of 10 nm. We have experimented with a transducer with 1.5 nm resolution and found essentially no improvement in the results presented below. A “top hat” with electrical feedthroughs (not pictured) is also affixed atop the apparatus to provide space for an extensometer to sit within the gas environment. An extensometer is valuable for long-term creep experiments since it provides temperature compensation. However, we have found the extensometer to be subject to significant resonance during forced oscillations, and therefore, it is removed from the apparatus during those experiments and not described in further detail here.

The load is measured by a load cell with a range of 9 kN and a repeatability of 1 N. The loading frame and loading column are designed for maximum loads of 5 kN. Due to the weight of the lower piston and piezoelectric actuator, there is a systematic background load of 98 N measured by the upper load cell.

C. High-temperature furnace and the chemical environment

As depicted in Fig. 1, the sample is heated with a gas-mixing tube furnace that encloses an alumina tube, the sample assembly, and the two SiC pistons. The top of the furnace tube is affixed to a water-cooled mounting bracket on the upper crosshead and the bottom to a water-cooled fitting with a frictionless seal for the bottom SiC piston to pass through. The maximum operating temperature is $\sim 1330^\circ\text{C}$ and is limited by the maximum power of the heating element of the furnace. The sample temperature is controlled within $\pm 0.1^\circ\text{C}$ using a K-type thermocouple placed at the height of the center of the samples, ~ 15 mm from the centerline of the loading column.

For future experiments on materials that are sensitive to the oxygen fugacity, a controlled ratio of CO_2 and CO will be fluxed through the furnace tube throughout the experiment. For most of the calibration experiments described below, the samples were stable in air at the conditions of interest, and therefore, modification of the chemical environment within the furnace was not necessary.

D. Characteristics of calibration samples

A variety of samples were used in the calibration tests described below. As our primary calibrant, we use single-crystal sapphire oriented for compression along the [0001] axis. Sapphire deformed in this orientation is ideal for calibrating the apparatus stiffness because of its well-characterized Young's modulus of 456 GPa (Cheng *et al.*, 2016 and Wang *et al.*, 2017) and lack of viscous deformation at room temperature (Firestone and Heuer, 1976). We tested a variety of sapphire crystals with different sample

dimensions (4, 6, and 8 mm in length) to examine the dependence of the apparatus compliance on sample size. All sapphire samples were 4 mm in diameter. Other samples tested include annealed, high-purity aluminum and acrylic, with diameters of 10 mm and lengths of 20 and 10 mm, respectively. The apparatus stiffness calibration experiments described below are sensitive to irregularities in the contact between interfaces in the loading column. The ends of all samples were ground flat and parallel with medium- and fine-grit sand paper (P300 and P1500, respectively), and superglue was used to ensure good contact between the sample and the two pistons at room temperature following the method by Takei and Karasawa (2014).

III. SENSITIVITY TESTING AND CALIBRATION

A. Timing error in data acquisition

To improve the capability of the apparatus to measure low magnitudes of attenuation, we must ensure the relative timing of different measured signals is as precise as possible. As illustrated in Fig. 2, an impulse generated by the piezoelectric actuator results in a near-instantaneous increase in both the position and the load. However, the recorded increase in position occurs slightly ahead of the recorded increase in load, which is an erroneous feature of our data acquisition system. To quantify this timing error, we conducted several tests consisting of a rapid 10-N increase in load and estimated the timing offset by cross-correlating the position and load signals. The measured timing error is $\sim 200\ \mu\text{s}$, which is independent of the sampling rate used for data acquisition. All datasets discussed below have been corrected for this timing error by shifting the position signal forward by $200\ \mu\text{s}$.

B. Resonant frequency

A factor that may add an additional complication to interpretation of attenuation experiments is resonance of the apparatus. We conducted several tests on single-crystal sapphire to estimate the resonant frequency of the loading frame and loading column, as illustrated in Fig. 3.

To conduct these tests, we applied an impulse directly to the loading frame by increasing the load instantaneously from 1 to 4 kN.

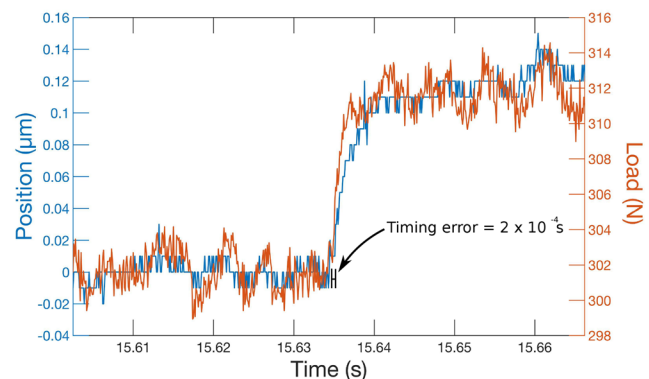


FIG. 2. Rapid load increase to measure the timing error between the position and load signals. The timing error estimated by cross-correlation is 2×10^{-4} s. These data were collected with a sampling rate of 10 kHz.

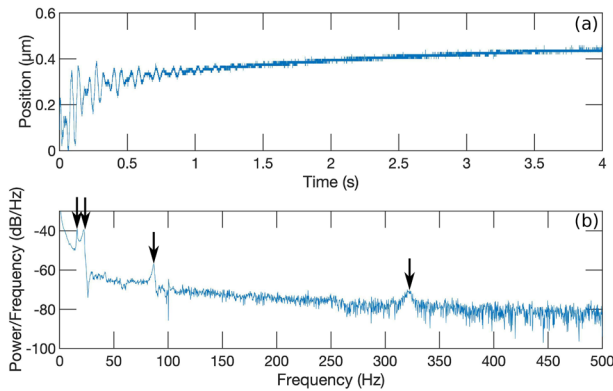


FIG. 3. Rapid load increase (from 1 to 4 kN) to evaluate the resonance of the apparatus. (a) Displacement measured as a function of time at room temperature just after the load increases. (b) The power spectrum of the time series presented in (a). The arrows indicate apparent resonant frequencies (16, 20, 90, and 320 Hz).

The recorded displacement and its power spectrum are presented in Fig. 3. These results indicate that the fundamental resonance occurs at a frequency of 16 Hz, with additional peaks at ~20, 90, and 320 Hz. Therefore, we explicitly avoid these (and nearby) frequencies when conducting forced oscillation tests to measure the complex compliance of the apparatus.

C. Methods for calculating attenuation

An additional consideration in conducting attenuation experiments is the method by which the data are processed. We evaluated four different methods to calculate attenuation, Q^{-1} . A common method for calculation of attenuation (e.g., Jackson and Faul, 2010; McCarthy and Cooper, 2016; and Takei et al., 2011) is from the phase shift between the stress and strain signals. An applied oscillating stress, $\sigma(t) = \sigma_0 \exp(i2\pi ft)$, results in an oscillating strain, $\epsilon(t) = \epsilon_0 \exp(i2\pi ft - \delta)$, where a subscript 0 indicates the amplitude, f is the temporal frequency, and δ is the phase lag in radians. The attenuation can be directly calculated from the phase lag by

$$Q^{-1} = \tan(\delta). \quad (1)$$

The apparent modulus can also be calculated by

$$E = \frac{\sigma_0}{\epsilon_0}, \quad (2)$$

where σ_0 and ϵ_0 are the maximum stress and maximum strain, respectively. We note that for linear viscoelastic materials, σ_0 and ϵ_0 scale together such that E is a constant but for nonlinear viscoelastic materials, Q^{-1} and E are functions of σ_0 . Three additional methods can be used to estimate the attenuation from the same dataset using the geometry of an elliptical Lissajous loop (Fig. 4; Lakes, 2009, pp. 60–62).

In reference to Fig. 4, the second method of calculating attenuation utilizes the intersection of the Lissajous loop with the strain axis, A , and the strain magnitude at the maximum stress, C ,

$$Q^{-1} = \frac{A}{C}. \quad (3)$$

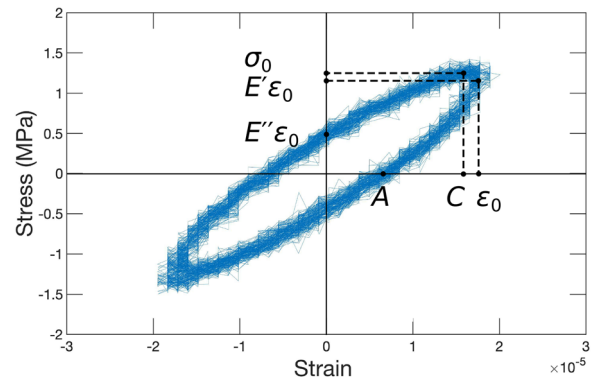


FIG. 4. Typical example of a stress–strain curve from a forced-oscillation measurement on single-crystal sapphire. ~100 cycles are represented in this figure. These data have not been corrected for the distortion of the apparatus. Forced oscillation was imposed at 60 Hz with a 16 MPa bias stress. Note that the bias stress and any apparent creep have been removed from these data.

Third, the attenuation can be calculated using the ratio of the imaginary component of the complex modulus, E'' , to the real component of the complex modulus, E' ,

$$Q^{-1} = \frac{E''}{E'}, \quad (4)$$

where E'' and E' can be determined from the intersection of the Lissajous loop with the stress axis and the stress magnitude at the maximum strain, respectively.

Finally, the area within the Lissajous loop can be evaluated by integrating the stress–strain data. The attenuation is given by $2/\pi$ multiplied by the ratio of one quarter of the total dissipated energy over a full cycle to the stored energy in a quarter cycle,

$$Q^{-1} = \frac{2 \frac{1}{4} \int_0^{\frac{1}{4}} \sigma \frac{d\epsilon}{dt} dt}{\pi \int_0^{\frac{1}{4}} \sigma \frac{d\epsilon}{dt} dt}. \quad (5)$$

Although these methods of calculating attenuation are theoretically equivalent, differences can arise associated with methods of data processing. The phase shift can be estimated by cross-correlation methods or Fourier analysis. In contrast, estimates of attenuation based on the Lissajous loop can be made by hand from plots, such as those in Fig. 4, by taking the mean of A , C , E'' , and E' for each loop or by finding a best-fit ellipse. We have compared all of these methods using the data described in Sec. III E and find that calculated values of attenuation are reasonably insensitive to the method used, only differing by 25% at most. Fourier analysis to find the phase shift has been chosen in analyzing the attenuation data presented below. We examine 30–100 cycles in each Fourier analysis.

D. Complex compliance of the apparatus

In the apparatus configuration described above, displacement of the sample is inferred from measurements of the piston displacement referenced to the loading frame (i.e., with the linear encoder). Therefore, we apply a compliance correction to remove the distortion of the apparatus from the total measured distortion.

To estimate the complex compliance of the apparatus, we conducted several forced-oscillation tests on single-crystal sapphire (an example is presented in Fig. 4).

Although this apparatus is designed for investigating viscoelasticity at high temperatures, we only conduct calibration experiments at room temperature. This decision is based on the critical influence of the piston–sample contacts. The initial contact is inherently rough, which adds an additional compliance to the system due to deformation of asperities. For this reason, we use superglue (as described above) to provide a rigid contact between the sample and pistons. This approach clearly is not available at high temperatures. For tests at high temperature on materials of interest (rather than materials for calibration), an initial stage of creep at the beginning of the experiment allows asperities to flow and good sample–piston contact to be achieved. However, this approach is also not available for calibration runs at high temperatures because of the sapphire’s strong resistance to creep (Firestone and Heuer, 1976). We emphasize that only the SiC pistons reach elevated temperatures, and therefore, we only expect temperature to affect the apparatus compliance through the change in modulus of SiC. Young’s modulus of SiC is only reduced by ~5% by increasing from room temperature to 1530 °C (Fukuhara and Abe, 1993). Therefore, even if all of the apparatus compliance results from the SiC pistons and all of their length are brought to the same elevated temperature (the hot zone of the furnace is actually only ~8 cm in length), we expect less than a 5% increase in the measured apparatus compliance.

To measure the apparatus compliance, we follow the work by Takei *et al.* (2011) and treat the apparatus and sample as a two-spring system connected in mechanical series (Takei *et al.*, 2011). Takei *et al.* (2011) defined three complex spring compliances, given by

$$C_{\text{observed}}^* = \left(\frac{L}{S} \right) J_{\text{observed}}^* \quad (6)$$

$$C_{\text{sample}}^* = \left(\frac{L}{S} \right) J_{\text{sample}}^* \quad (7)$$

$$C_{\text{apparatus}}^* = C_{\text{observed}}^* - C_{\text{sample}}^* \quad (8)$$

where C is a spring compliance (units of length/force), L is the sample length, S is the cross-sectional area of the sample, J is the compliance (units of inverse stress), “*” indicates a complex variable, and the subscripts indicate the component of the system with which the value is associated. Note that for nonlinear viscoelastic materials, either the real or imaginary component or both components of the complex compliance are a function of the stress amplitude.

For our calibrations, C_{sample}^* corresponds to the known value for sapphire (Pezzotti *et al.*, 1997 and Wachtman and Lam, 1959), and C_{observed}^* corresponds to the value measured in the experiment. The difference between C_{observed}^* and C_{sample}^* , according to Eq. (8), yields the complex spring compliance of the apparatus.

Calibration experiments were conducted over ranges of frequencies, load amplitudes, bias stresses, and sample dimensions, with multiple repeat tests at each set of conditions. Figure 5 presents the apparatus spring compliance as a function of frequency and load amplitude. Over the range of conditions tested, the real part of the apparatus spring compliance is on the order of 4 nm/N with

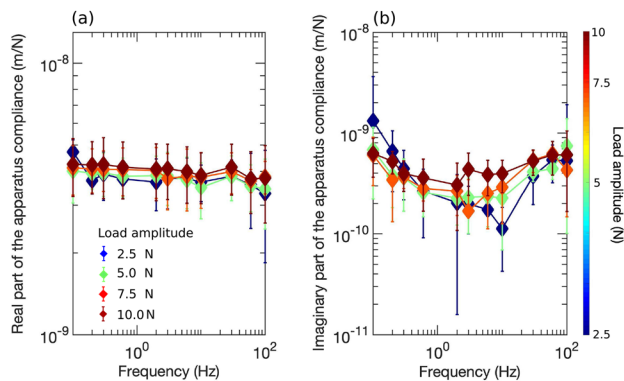


FIG. 5. $C_{\text{apparatus}}^*$ measured as a function of frequency and load amplitude at room-temperature using single-crystal sapphire as the calibration standard. (a) The real part of the apparatus compliance. (b) The imaginary part of the apparatus compliance. Multiple measurements are made at each value of frequency and amplitude. The symbol indicates the mean value, and the error bars denote one standard deviation.

relatively little dependence on frequency. The imaginary part of the apparatus spring compliance is generally <1 nm/N and exhibits a subtle, negative frequency dependence at low frequencies. Only the imaginary part of the apparatus compliance exhibits a dependence on the load amplitude, with high amplitudes associated with increased compliance, primarily at intermediate frequencies.

We also examined the dependence of the apparatus compliance on the magnitude of the bias stress. As illustrated in Fig. 6, we did not observe a systematic dependence of either the real or imaginary parts of the compliance on the bias stress.

Finally, we examined the dependence of the apparatus compliance on the sample length. As illustrated in Fig. 7, the real part of the apparatus compliance exhibits a systematic dependence on the sample length, with greater compliance as the sample length is decreased. We interpret this dependence to reflect the increase in length of the effective loading column as the lower piston is raised by the worm gear to accommodate shorter samples. However, the proportional

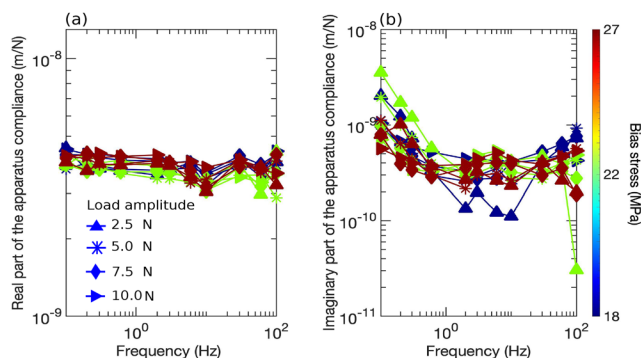


FIG. 6. $C_{\text{apparatus}}^*$ measured as a function of frequency and bias stress at room-temperature using single-crystal sapphire as the calibration standard, with a fixed sample length. (a) The real part of the apparatus compliance. (b) The imaginary part of the apparatus compliance. Both (a) and (b) demonstrate that the compliance of the apparatus is essentially independent of the bias stress.

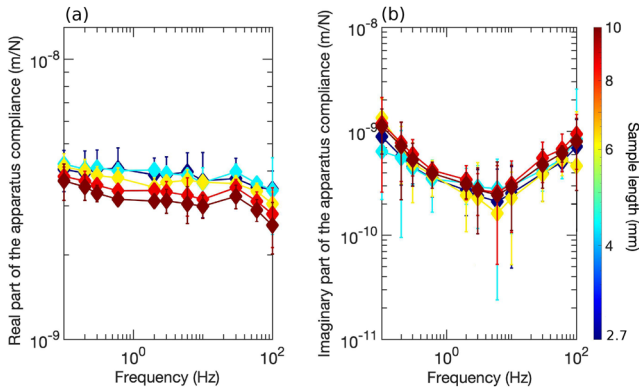


FIG. 7. C^* _{apparatus} measured as a function of frequency at room-temperature using single-crystal sapphire with different sample lengths as the calibration standard. (a) The real part of the apparatus compliance. (b) The imaginary part of the apparatus compliance. Multiple measurements are made at each value of frequency and sample length. The symbols indicate the mean values, and the error bars denote two standard deviations.

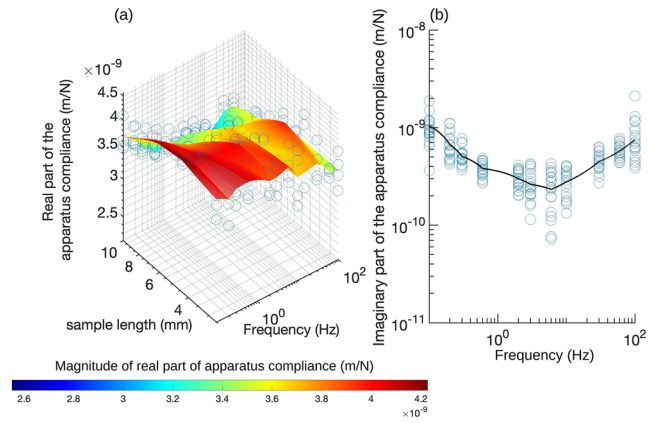


FIG. 8. (a) Interpolated surface describing the dependence of the real part of the apparatus compliance on sample length and frequency. (b) The interpolated curve describing the dependence of the imaginary component of the apparatus compliance on frequency. In (a) and (b), blue circles indicate individual measurements.

change in length of the sample (~30% at maximum) is much larger than the proportional change in length of the piston (~2% at maximum), which suggests a nonlinear relationship between apparatus compliance and piston length. The lack of dependence of the imaginary component of the compliance on the sample length suggests that components other than the pistons are likely responsible for any relaxation. A likely source of the dissipation is the linear bearings for the guide rails on the lower piston.

To define a best-fit apparatus compliance, we fit the data from these calibration experiments on sapphire to individual functions for the real and imaginary components. As demonstrated in Figs. 5–7, the real component of the compliance is dependent on the frequency and sample length, whereas the imaginary component of the apparatus compliance is primarily dependent only on the frequency. The functions fit to the real and imaginary components of the compliance are, therefore, constrained to only depend on those quantities. Fitting functions are determined by taking the mean of the compliances at a given set of independent variables and then conducting a linear interpolation among those means. Figure 8(a) presents the interpolated surface to the real component of the compliance and illustrates the tradeoff between frequency and sample length. Figure 8(b) illustrates the interpolated curve to the imaginary component of the compliance.

E. Example measurements on aluminum and acrylic

To evaluate the ability of the apparatus and data processing method to estimate the attenuation, Q^{-1} , and Young’s modulus, E , of a given sample, we made a variety of measurements on materials for which viscoelastic properties have been previously investigated. We first calculated Q^{-1} and E using Eqs. (1)–(3). We then use the relations

$$E = (J'^2 + J''^2)^{-\frac{1}{2}}, \quad (9)$$

$$Q^{-1} = \frac{J''}{J'} \quad (10)$$

to find J' and J'' , which are the real and imaginary components of the complex compliance, respectively. With our measured values of the apparatus compliance, C^* _{apparatus}, we correct these observed spring compliances according to

$$J^*_{\text{sample}} = J^*_{\text{observed}} - \frac{S}{L} C^*_{\text{apparatus}}. \quad (11)$$

We use this method to estimate E and Q^{-1} over a wide range of frequencies for annealed polycrystalline aluminum and acrylic, as depicted in Fig. 9. As suggested by Eq. (11), the higher-quality, less compliant aluminum results in a much smaller signal, and therefore, the compliance correction is more substantial than for acrylic. We also assess the experimental error of our measurements by propagating the errors in estimation of the apparatus compliance through our calculation of E and Q^{-1} . Error bars in Fig. 9 represent two standard deviations in the values of the apparatus compliance, for which error in attenuation measurement is approximately one order of magnitude and error in Young’s modulus is ~10% for acrylic and 25% for aluminum.

Although these error estimates are relatively large, our measurements are consistent with previous results for aluminum (Esnouf and Fantozzi, 1981; Iwasaki, 1980, 1984; Rivière, 2003; Takei et al., 2011; and Wei et al., 2002) and acrylic (Fukada, 1954; Takei et al., 2011; and Yee and Takemori, 1982). We conducted tests on these materials at the smallest bias stress (~0.1 MPa) and stress amplitudes (~0.05 MPa) possible to best match the conditions of experiments described in the available literature. Our measured magnitudes of attenuation and Young’s modulus are generally within the error of previously published data, and the variability among previous studies is comparable in magnitude to our confidence limits. Furthermore, our experiments capture the frequency dependence of attenuation in aluminum and acrylic exhibited in previous studies. We also reasonably capture the frequency dependence of Young’s modulus in acrylic. However, only one dataset is available, to our knowledge, for Young’s modulus in annealed

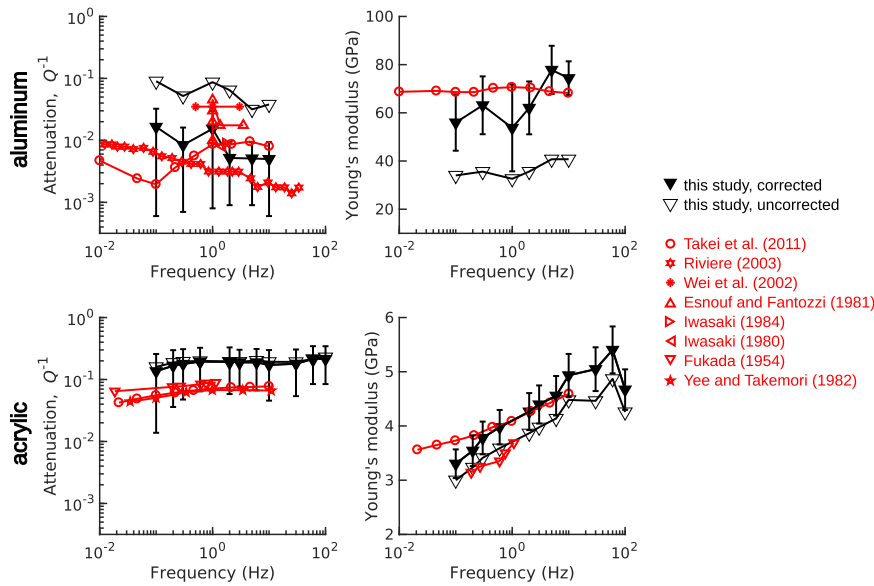


FIG. 9. Attenuation, Q^{-1} , and Young's modulus measured as a function of frequency for aluminum and acrylic at room temperature. The black open and solid symbols indicate our measurements of the attenuation and modulus before and after correction for the apparatus compliance, respectively. Error bars indicate two standard deviations of repeat measurements. Red symbols indicate values from other publications conducted at similar stress amplitudes to our experiments.

aluminum in the frequency range of interest (Takei *et al.*, 2011), which does exhibit a smaller frequency dependence than we observe, although those data were collected at conditions with relatively poor signal to noise, as discussed below. The large frequency dependence of aluminum observed here is larger than that expected from the Kramers–Kronig relations for linear viscoelastic materials (e.g., Lakes, 2009, p. 64). This discrepancy may result from the activity of some nonlinear processes in our aluminum samples or from the relatively large errors on our measurements of Young's modulus in aluminum (Fig. 9).

IV. DISCUSSION

A. Limits to measurement of attenuation and modulus

With a quantitative understanding of the complex compliance of this apparatus, we can place bounds on the magnitudes of sample compliances that are reasonably measurable. Takei *et al.* (2011) suggested that accurate measurements of the viscoelastic properties of a material require displacements associated with distortion of the apparatus to be smaller than the displacements associated with distortion of the sample, that is, $C'_{\text{sample}} > C'_{\text{apparatus}}$ and $C''_{\text{sample}} > C''_{\text{apparatus}}$. We modify these criteria by suggesting that the apparatus spring compliance can be larger than the sample spring compliance as long as the apparatus compliance is precisely known and suitably reproducible. Therefore, we suggest that the spring compliance of the sample must be larger than that of the error in the apparatus compliance, $C^*_{\text{app,error}}$, that is, $C'_{\text{sample}} > C^*_{\text{app,error}}$ and $C''_{\text{sample}} > C^*_{\text{app,error}}$. In this context, we define $C^*_{\text{app,error}}$ as one standard deviation of the measurements of $C^*_{\text{apparatus}}$, which corresponds to 3.4×10^{-10} and 2.3×10^{-10} m/N for the real and imaginary component, respectively. We can therefore calculate the critical sample Young's modulus, E_c , and the critical sample attenuation, Q^{-1} , which act as a maximum and minimum value, respectively, that can be reliably measured with this apparatus. These values are calculated

from $C^*_{\text{app,error}}$ by taking the sample dimensions into account,

$$Q_c^{-1} = E \frac{S}{L} C''_{\text{app,error}}, \quad (12)$$

$$E_c = \frac{L}{SC'_{\text{app,error}}}. \quad (13)$$

These limits are plotted for standard sample sizes in Fig. 10.

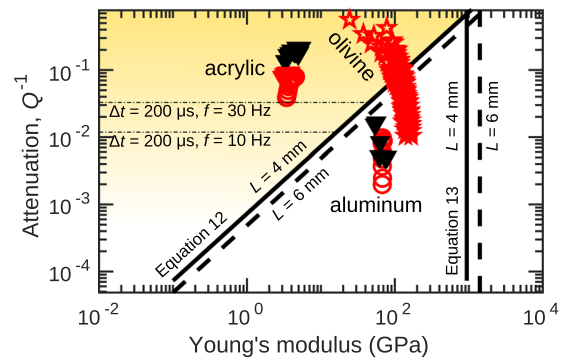


FIG. 10. Bounds on reliable measurements of attenuation and Young's modulus by the criterion suggested in this study [Eqs. (12) and (13)]. The shaded area indicates the values of the sample attenuation and sample modulus that result in sample displacements larger than the error in the apparatus displacement. These bounds are dependent on the sample length, L . Also presented are example values of E and Q^{-1} for aluminum (Takei *et al.*, 2011), acrylic (Fukada, 1954 and Takei *et al.*, 2011), and olivine (Jackson and Faul, 2010; Faul and Jackson, 2015; and Cline *et al.*, 2018). Markers are as in Fig. 9, with black triangles indicating our measurements and red symbols indicating previously published results. The horizontal dashed-dotted lines indicate a minimum value of Q^{-1} , above which the predicted time delay associated with dissipation, Δt , is greater than a timing error of 200 μs , which is dependent on the oscillation frequency, f .

An additional constraint arises from the measured timing error between the load and displacement signals (Fig. 2). The horizontal, dashed-dotted lines in Fig. 10 indicate a minimum measurable value of Q^{-1} , above which the predicted time delay between the load and displacement signals, Δt , is greater than that caused by a timing error of 200 μs . These minima in Q^{-1} vary linearly with the oscillation frequency, with an increase in frequency from 10 to 30 Hz leading to an increase of a factor of 3 in the minimum measurable attenuation. Although this additional constraint limits the maximum frequencies we can work with, we note that most previous apparatus designed for working at high homologous temperatures in geological materials are limited to much lower frequencies (<10 Hz).

Our apparatus also has a limit on the minimum frequency at which usable measurements can be obtained, which is primarily determined by the thermal stability of the apparatus. Because the displacement measurement is not thermally compensated, any thermal expansion and contraction of the loading frame and loading column influence the measured displacements. Thermal fluctuations (<1 °C) associated with the furnace control are apparent at a frequency of $\sim 10^{-2}$ Hz. Therefore, we currently limit measurements to 10^{-1} Hz and above.

Also depicted in Fig. 10 are the values for E and Q^{-1} of aluminum and acrylic. According to Eqs. (12) and (13), attenuation and Young's modulus of acrylic is well within the measurable range, which is confirmed by the smaller error bars for acrylic in Fig. 9. In contrast, the published values of attenuation and Young's modulus for aluminum are below our threshold for precise measurement, which is in agreement with the large error bars for measurements of aluminum in Fig. 9 and may be the source of the large apparent dispersion.

As an example of applicability to geological materials, Fig. 10 also compares our constraints to previous measurements of attenuation in olivine (Cline *et al.*, 2018; Faul and Jackson, 2015; and Jackson and Faul, 2010). Young's modulus of olivine is clearly accessible with this apparatus, although only about half of the previously published olivine data (solid red triangles) lie within the range of measurable values of attenuation. For relatively stiff geological materials, this analysis suggests this apparatus is only capable of precisely measuring relatively high levels of attenuation ($>10^{-1}$) unless substantially larger samples are used. We suggest that measurements of attenuation will be most successful if conditions are chosen to maximize the dissipation of the sample, such as at high temperatures, fine-grain sizes, or high stress amplitudes.

B. Comparison to other apparatus

A variety of apparatus have been developed to measure the attenuation of geological materials at elevated temperatures with forced oscillations (Gribb and Cooper, 1998b; Gueguen *et al.*, 1989; Jackson and Paterson, 1993; and Sundberg and Cooper, 2010). These apparatus were primarily designed to investigate attenuation in the linear regime for application to seismic-wave attenuation. However, these apparatus designs are not able to apply a bias stress, which means they are unable to measure attenuation while the material is simultaneously creeping. Thus, to investigate the effect of defects related to creep (e.g., dislocations) on attenuation, samples must be predeformed in a separate experiment prior to measurement of attenuation. For example, to investigate the role of

dislocation density on attenuation in olivine, Gueguen *et al.* (1989) measured the attenuation of single-crystal Fo_{100} (100% forsterite) predeformed in a 1-atm creep apparatus at 20 MPa differential stress, and Farla *et al.* (2012) measured the attenuation of aggregates of Fo_{90} (iron-bearing forsterite) predeformed at a differential stress of 230 MPa. A downside of this approach is that, during subsequent viscoelastic experiments at high temperatures, recovery acts to modify the specific arrangement of dislocations, the dislocation density, and the internal stress distribution as the attenuation is measured.

There are several existing apparatus designed for geological applications that do allow a high bias stress to be applied during oscillatory experiments, although they are limited to low temperatures. Takei *et al.* (2011) described an apparatus that allows creep and attenuation to be measured simultaneously at temperatures up to 50 °C. This apparatus has been specifically used for characterizing organic, crystalline materials that act as rock analogs. McCarthy and Cooper (2016) described viscoelastic measurements with a high bias stress utilizing a servomechanical apparatus designed for cryogenic conditions, and their experiments on ice revealed nonlinear behavior associated with dislocation activity.

The apparatus that we introduce here provides new and key capabilities for measuring the viscoelasticity of geological materials. This apparatus is capable of conducting forced-oscillation tests in tandem with an appreciable bias stress (maximum loads of 5 kN) while at temperatures up to 1330 °C in a controlled chemical environment. We are, therefore, able to explore amplitude-dependent, nonlinear viscoelasticity at high homologous temperatures in minerals with high melting temperatures. The ability to apply a bias stress allows the viscoelastic properties to be investigated during creep, including that as the microstructure evolves during the initial increments of transient creep. Furthermore, we can potentially apply a low-frequency oscillation to the bias stress, which has been an extremely valuable technique for investigating dislocation dynamics in metals at low temperatures (e.g., Gremaud and Bujard, 1985). We acknowledge that a uniaxial stress state (i.e., no confining pressure) may result in microcracking in some materials at high bias stresses. Therefore, if microcracking is not a target process in future investigations, potential samples for investigation include crack-free single crystals and extremely fine-grained polycrystalline samples.

V. CONCLUSIONS

A high-temperature, uniaxial creep apparatus has been developed in this study to investigate the nonlinear attenuation of crystalline materials over a wide range of temperature (25–1300 °C), using forced-oscillations. This apparatus is primarily designed for applying oscillatory compressional stress to estimate attenuation and Young's modulus. This apparatus allows us to apply a high bias stress in addition to forced oscillations, enabling us to investigate the effect of creep-derived defects (e.g., dislocations) on attenuation and modulus.

We performed a variety of calibration tests, including quantifying the timing errors in the data acquisition system, the resonant frequencies of the apparatus, and the complex compliance of the apparatus. Based on the results from the calibration tests conducted

on single-crystal sapphire, the real part of the apparatus compliance is on the order of 4 nm/N with relatively little dependence on frequency. The imaginary part of the apparatus compliance is generally <1 nm/N, illustrating a subtle negative frequency dependence at low frequencies. The real part of the apparatus compliance exhibits a systematic dependence on the sample length, with greater compliance as the sample length is decreased. There is no systematic dependence of either the real or imaginary part of the compliance on the bias stress. We define best-fit functions to allow the real and imaginary component of the compliance to be estimated at any frequency, amplitude, or sample length within the ranges explored here.

With subsequent measurements of the compliance of aluminum and acrylic, we demonstrate that correction of data for the apparatus compliance yields reasonable measurements of Q^{-1} and E . We have constrained the upper limit of E and the lower limit of Q^{-1} that can be accurately measured.

SUPPLEMENTARY MATERIAL

See the [supplementary material](#) for a table of all compliance measurements made as part of the apparatus calibration.

ACKNOWLEDGMENTS

The authors wish to acknowledge the considerable effort from Physik Instrumente in the design and construction of this apparatus, including Geraint Green, John Hopkins, and Huw Prosser. Invaluable design and construction input was also provided by Jamie Long and James King in the Earth Sciences Workshop at the University of Oxford. This manuscript was improved by the insightful and constructive comments of two anonymous reviewers. R.C. acknowledges support from the Great Britain-China Educational Trust, Mineralogical Society of Great Britain & Ireland, and the Linacre Travel Fund. L.H. and C.T. acknowledge support from the Natural Environment Research Council (Grant No. 1710DG008/JC4). L.H. and D.W. acknowledge support from the Natural Environment Research Council (Grant No. NE/M000966/1). D.W. acknowledges support from the Netherlands Organisation for Scientific Research, User Support Programme Space Research (Grant No. ALWGO.2018.038). L.H. recognizes funds used to develop the apparatus from the John Fell Fund at the University of Oxford.

DATA AVAILABILITY

The data that support the findings of this study are available from the corresponding author upon reasonable request.

REFERENCES

- Agata, R., Barbot, S. D., Fujita, K., Hyodo, M., Iinuma, T., Nakata, R., Ichimura, T., and Hori, T., "Rapid mantle flow with power-law creep explains deformation after the 2011 Tohoku mega-quake," *Nat. Commun.* **10**, 1385 (2019).
- Bai, Q. and Kohlstedt, D. L., "High-temperature creep of olivine single crystals III. Mechanical results for unbuffered samples and creep mechanisms," *Philos. Mag. A* **66**, 1149–1181 (1992).
- Cheng, T. S., Davies, A., Summerfield, A., Cho, Y., Cebula, I., Hill, R. J. A., Mellor, C. J., Khloubystov, A. N., Taniguchi, T., Watanabe, K., Beton, P. H., Foxon, C. T., Eaves, L., and Novikov, S. V., "High temperature MBE of graphene on sapphire and hexagonal boron nitride flakes on sapphire," *J. Vac. Sci. Technol. B* **34**, 02L101 (2016).
- Cline, C. J. II, Faul, U. H., David, E. C., Berry, A. J., and Jackson, I., "Redox-influenced seismic properties of upper-mantle olivine," *Nature* **555**, 355–358 (2018).
- Esnouf, C. and Fantozzi, G., "Medium temperature internal friction in high purity f.c.c. and h.c.p. metals," *J. Phys. Colloq.* **42**, C5-445 (1981).
- Farla, R. J. M., Jackson, I., Fitz Gerald, J. D., Faul, U. H., and Zimmerman, M. E., "Dislocation damping and anisotropic seismic wave attenuation in Earth's upper mantle," *Science* **336**, 332–335 (2012).
- Faul, U. and Jackson, I., "Transient creep and strain energy dissipation: An experimental perspective," *Annu. Rev. Earth Planet. Sci.* **43**, 541–569 (2015).
- Firestone, R. F. and Heuer, A. H., "Creep deformation of 0° sapphire," *J. Am. Ceram. Soc.* **59**, 24–29 (1976).
- Freed, A. M., Hirth, G., and Behn, M. D., "Using short-term postseismic displacements to infer the ambient deformation conditions of the upper mantle," *J. Geophys. Res.: Solid Earth* **117**, B01409, <https://doi.org/10.1029/2011jb008562> (2012).
- Fukada, E., "The relation between dynamic elastic modulus, internal friction, creep and stress relaxation in polymethyl methacrylate," *J. Phys. Soc. Jpn.* **9**, 786–789 (1954).
- Fukuhara, M. and Abe, Y., "High-temperature elastic moduli and internal frictions of α -SiC ceramic," *J. Mater. Sci. Lett.* **12**, 681–683 (1993).
- Gremaud, G. and Bujard, M., "Recent progress in dislocation studies using bias stress experiments," *J. Phys. Colloq.* **46**, C10-315–C10-320 (1985).
- Gremaud, G., Bujard, M., and Benoit, W., "The coupling technique: A two-wave acoustic method for the study of dislocation dynamics," *J. Appl. Phys.* **61**(5), 1795–1805 (1987).
- Gribb, T. T. and Cooper, R. F., "A high-temperature torsion apparatus for the high-resolution characterization of internal friction and creep in refractory metals and ceramics: Application to the seismic-frequency, dynamic response of Earth's upper mantle," *Rev. Sci. Instrum.* **69**, 559–564 (1998).
- Gribb, T. T. and Cooper, R. F., "Low-frequency shear attenuation in polycrystalline olivine: Grain boundary diffusion and the physical significance of the Andrade model for viscoelastic rheology," *J. Geophys. Res.: Solid Earth* **103**, 27267–27279, <https://doi.org/10.1029/98jb02786> (1998).
- Gueguen, Y., Darot, M., Mazot, P., and Woignard, J., " Q^{-1} of forsterite single crystals," *Phys. Earth Planet. Inter.* **55**, 254–258 (1989).
- Iwasaki, K., "Internal friction peaks of cold worked pure aluminum and its dilute alloys," *J. Phys. Soc. Jpn.* **49**, 271–278 (1980).
- Iwasaki, K., "High-temperature internal friction peaks of pure aluminum single-, bi-, and polycrystals measured with an inverted flexure pendulum," *Phys. Status Solidi A* **81**, 485–496 (1984).
- Jackson, I. and Faul, U. H., "Grainsize-sensitive viscoelastic relaxation in olivine: Towards a robust laboratory-based model for seismological application," *Phys. Earth Planet. Inter.* **183**, 151–163 (2010).
- Jackson, I. and Paterson, M. S., "A high-pressure, high-temperature apparatus for studies of seismic wave dispersion and attenuation," *Pure Appl. Geophys.* **141**, 445–466 (1993).
- Kaiser, G. and Pechhold, W., "Dynamic-mechanical investigations for the study of dislocation motion during plastic flow," *Acta Metall.* **17**, 527–537 (1969).
- Lakes, R. S., *Viscoelastic Materials* (Cambridge University Press, 2009).
- Li, L. and Weidner, D. J., "Energy dissipation of materials at high pressure and high temperature," *Rev. Sci. Instrum.* **78**, 053902 (2007).
- Masuti, S., Barbot, S. D., Karato, S.-I., Feng, L., and Banerjee, P., "Upper-mantle water stratification inferred from observations of the 2012 Indian Ocean earthquake," *Nature* **538**, 373–377 (2016).
- McCarthy, C. and Cooper, R. F., "Tidal dissipation in creeping ice and the thermal evolution of Europa," *Earth Planet. Sci. Lett.* **443**, 185–194 (2016).
- McCarthy, C., Takei, Y., and Hiraga, T., "Experimental study of attenuation and dispersion over a broad frequency range: 2. The universal scaling of polycrystalline materials," *J. Geophys. Res.: Solid Earth* **116**, B09207, <https://doi.org/10.1029/2011jb008384> (2011).

- Moore, J. D. P., Yu, H., Tang, C.-H., Wang, T., Barbot, S., Peng, D., Masuti, S., Dauwels, J., Hsu, Y.-J., Lambert, V., Nanjundiah, P., Wei, S., Lindsey, E., Feng, L., and Shibasaki, B., "Imaging the distribution of transient viscosity after the 2016 M_w 7.1 Kumamoto earthquake," *Science* **356**, 163–167 (2017).
- Pezzotti, G., Ota, K., and Kleebe, H.-J., "Viscous slip along grain boundaries in chlorine-doped silicon nitride," *J. Am. Ceram. Soc.* **80**, 2341–2348 (1997).
- Qiu, Q., Moore, J. D. P., Barbot, S., Feng, L., and Hill, E. M., "Transient rheology of the Sumatran mantle wedge revealed by a decade of great earthquakes," *Nat. Commun.* **9**, 995 (2018).
- Rivière, A., "Measurement of high damping: Techniques and analysis," *J. Alloys Compd.* **355**, 201–206 (2003).
- Sapozhnikov, K. V. and Kustov, S. B., "Effect of temperature on the amplitude dependences of the acoustoplastic effect and internal friction during deformation of crystals," *Philos. Mag. A* **76**, 1153–1168 (1997).
- Sundberg, M. and Cooper, R. F., "A composite viscoelastic model for incorporating grain boundary sliding and transient diffusion creep; correlating creep and attenuation responses for materials with a fine grain size," *Philos. Mag.* **90**, 2817–2840 (2010).
- Takei, Y., Fujisawa, K., and McCarthy, C., "Experimental study of attenuation and dispersion over a broad frequency range: I. The apparatus," *J. Geophys. Res.: Solid Earth* **116**, 65, <https://doi.org/10.1029/2011jb008382> (2011).
- Takei, Y. and Karasawa, F., "Temperature, grain size, and chemical controls on polycrystal anelasticity over a broad frequency range extending into the seismic range," *J. Geophys. Res.: Solid Earth* **119**, 5414, <https://doi.org/10.1002/2014jb011146> (2014).
- Twiss, R. J., "Variable sensitivity piezometric equations for dislocation density and subgrain diameter and their relevance to olivine and quartz," in *Mineral and Rock Deformation: Laboratory Studies*, AGU Geophysical Monographs (AGU, 1986), Vol. 36, pp. 247–263.
- Wachtman, J. B., Jr. and Lam, D. G., Jr., "Young's modulus of various refractory materials as a function of temperature," *J. Am. Ceram. Soc.* **42**, 254–260 (1959).
- Wallis, D., Hansen, L. N., Kumamoto, K. M., and Thom, C. A., "Dislocation interactions during low-temperature plasticity of olivine and their impact on the evolution of lithospheric strength," *Earth Planet. Sci. Lett.* **543**, 116349 (2020).
- Wang, J., Guo, B., Zhao, Q., Zhang, C., Zhang, Q., Chen, H., and Sun, J., "Dependence of material removal on crystal orientation of sapphire under cross scratching," *J. Eur. Ceram. Soc.* **37**, 2465–2472 (2017).
- Wei, J. N., Cheng, H. F., Zhang, Y. F., Han, F. S., Zhou, Z. C., and Shui, J. P., "Effects of macroscopic graphite particulates on the damping behavior of commercially pure aluminum," *Mater. Sci. Eng., A* **325**, 444–453 (2002).
- Yee, A. F. and Takemori, M. T., "Dynamic bulk and shear relaxation in glassy polymers. I. Experimental techniques and results on PMMA," *J. Polym. Sci., Polym. Phys. Ed.* **20**, 205–224 (1982).